Global Ground Motion Prediction Equation for Shallow Crustal Regions

Vladimir Graizer,[a] M.EERI, **Erol Kalkan,**[b] M.EERI, **and Kuo-Wan Lin**[c]

The Graizer-Kalkan ground-motion prediction equation (GMPE) for peak ground acceleration (PGA) constitutes a series of filters, each of which represents a certain physical phenomenon affecting the radiation of seismic waves from the source. The performance of this GMPE is examined by using about 14,000 records from 245 worldwide shallow crustal events. The recorded data and predictions show an excellent match as far as 100 km from the fault. Beyond 100 km, the data generally show faster attenuation on the order of R_{rup}^{-4} due to a relatively low Q (as in the western United States) or slower attenuation on the order of $R_{rup}^{-1.5}$ due to a high Q (as in the central and eastern United States). An improved GMPE is developed to account for regional variations in ground motion attenuation. The The new GMPE produces a better match to recorded data up to 500 km from the fault. [DOI: 10.1193/1.4000140]

INTRODUCTION

In many active seismic regions, there are too few recorded ground motion data from a wide range of magnitudes to develop reliable regional ground-motion prediction equations (GMPEs). For seismic hazard studies in these regions, it is customary to import GMPEs developed for other, similar tectonic environments. For example, the previous generation of GMPEs based on the western U.S. ground motion data (e.g., Abrahamson and Silva 1997, Boore et al. 1997, Campbell 1997, Sadigh et al. 1997) was widely used worldwide for shallow crustal regions. Those previous models were based on limited ground motion data from active shallow tectonic regions, but the Next Generation Attenuation (NGA) project has now provided a more complete set of data. The NGA database, along with a number of additions (e.g., 2003 San Simeon and 2004 Parkfield earthquakes in California, and other small magnitude events from Turkey and Armenia), was used to develop the Graizer-Kalkan (GK-07) GMPE (Graizer and Kalkan 2007). This GMPE models the attenuation function as a combination of filters, where each filter represents a certain physical phenomenon affecting seismic radiation (e.g., magnitude scaling, shallow site effect, basin-response effect). This approach provides robustness and stability to a GMPE by separating the influence of each physical effect (Graizer and Kalkan 2011). Excellent performance of the GK-07 GMPE in estimating recorded ground motions from recent events in Italy, Turkey, and New Zealand is demonstrated by Celebi et al. (2010), Akkar et al. (2011), and Segou and Kalkan (2011). In this paper, the accuracy of the GK-07 in predicting peak ground accelerations from global shallow crustal events in the near-field (within 20 km of fault), mid-field (from 20 km to 100 km of fault), and far-field

[a] U.S. Nuclear Regulatory Commission, Washington, DC, Vladimir.Graizer@nrc.gov
[b] U.S. Geological Survey, Menlo Park, CA, ekalkan@usgs.gov
[c] U.S. Geological Survey, Golden, CO, klin@usgs.gov

Earthquake Spectra, Volume 29, No. 3, pages 1–15, August 2013; © 2013, Earthquake Engineering Research Institute

(from 100 km to 500 km of fault) is examined here by using about 14,000 ground motion data. Ground motion prediction at distances more than 200 km is particularly important for seismic hazard assessments of critical facilities (e.g., nuclear power plants).

GROUND MOTION DATABASE

In this study, ShakeMaps from the U.S. Geological Survey Atlas of ShakeMaps (http://earthquake.usgs.gov/earthquakes/shakemap/atlas.php) for Selected Global Earthquakes (referred to herein as the Global Atlas) were used to compile 13,992 peak ground acceleration (PGA) data from 245 worldwide shallow crustal events (see electronic Appendix). This database contains PGA values within 500 km of the fault from earthquakes having moment magnitudes (*M*) in the range of 4.2 to 7.9. The distribution of PGA values against *M*, closest fault distance (R_{rup}) and average shear-wave velocity in the upper 30 m (V_{S30}) is shown in Figure 1 for both the Global Atlas database and the extended NGA database used for the development of the GK-07. The Global Atlas database is more complete both at near- and far-field and is also more inclusive in terms of geological conditions and magnitude range covered.

At large distances, strong motion data is limited due to the trigger level of accelerographs. For example, the standard is 0.005 g on the horizontal component and 0.01 g on the vertical component for strong motion stations operated by the USGS's National Strong Motion Project. This may result in bias in the data because it is obtained at stations in which the recorded acceleration is higher than the threshold; this bias is larger at far distances where the recorded accelerations are low (Fukushima and Tanaka 1990). In order to avoid this bias, broadband data is used to fill the gaps at large distances in the Atlas Database.

GRAIZER-KALKAN GROUND MOTION PREDICTION MODEL: SUMMARY

The GK-07 model was developed using a modular-filter-based approach (Graizer and Kalkan 2007, 2011). In this approach, the following mathematical formulation represents a GMPE:

$$Y = G_1(M, F) \cdot G_2(M, R_{rup}) \cdot G_3(M, R_{rup}) \cdot G_4(V_{S30}) \cdot G_5(M, R_{rup}) \cdot \sigma_Y \tag{1}$$

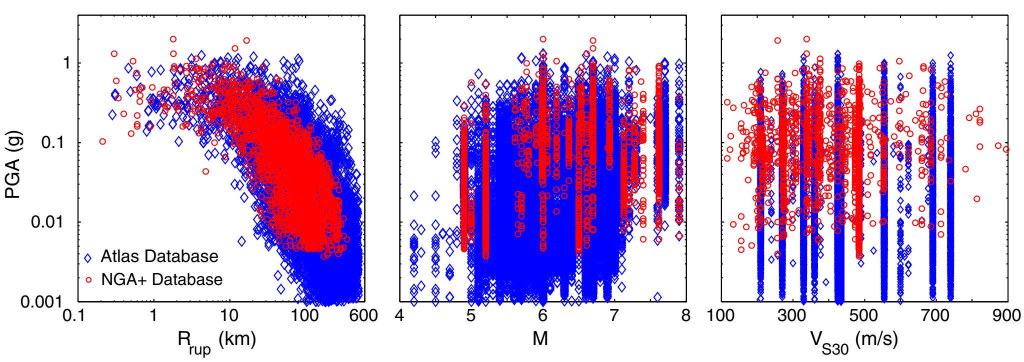

Figure 1. Distribution of PGA with respect to closest fault distance (R_{rup}), moment magnitude (*M*), and shear-wave velocity (V_{S30}) for the extended NGA (denoted as NGA+) and Global Atlas databases.

Y is the ground motion intensity measure (IM), and F is the style of faulting parameter. In this representation, each function (G_n) is a filter and in multiplicative form. Equation 1 is expressed in logarithmic space as:

$$\ln(Y) = \sum_n \ln[G_n] + \sigma_{ln(Y)} \tag{2}$$

Equation 2 is similar to the equation of a finite impulse response (FIR) filter, a digital filter characterized by its transfer function. Mathematical analysis of the transfer function can describe how it will respond to any input. For example, designing a filter consists of developing specifications appropriate to the problem and then producing a transfer function meeting those specifications. A similar approach for creating a GMPE as a transfer function is suggested. This modeling approach, in which a combination of filters is used in Equation 1, is analogous to the traditional seismological approach (e.g., Boore 2003), where the total spectrum of the motion at a site $Y(M_0, R, f)$ is split into four parts, with contributions from the earthquake source (E), path (P), site (S), and instrument or type of motion (I), as shown in Equation 3:

$$Y(M_0, R, f) = E(M_0, f) \cdot P(R, f) \cdot S(f) \cdot I(f) \tag{3}$$

When modeling a GMPE, using separate filters (G_n) offers the following advantages:

1. Each physical phenomenon on seismic radiation can be modeled by a separate filter as a function of independent physical parameters (e.g., M, R_{rup}, V_{S30}). This brings physical meaning to each filter and, consequently, more connection with theoretical seismology.
2. Instead of fitting an empirical predictive equation to the entire ground motion database via single- or two-stage regression, a more flexible filter-based approach is used. This approach allows for sequential data fitting via nonlinear optimization (see, e.g., Graizer and Kalkan 2007, 2009).
3. Use of separate filters also eliminates a need to search for a complex and purely empirical equation that fits data at all distances (to be discussed in detail later).

As shown in Figure 2, the first filter G_1 of our model is a scaling function for magnitude and style of faulting; G_2 models ground motion distance attenuation; G_3 is the correction function for (i) ground motion attenuation at intermediate distances, and (ii) deep sediment (basin) effects; G_4 is the correction function for shallow site effects. Separate filters can represent the amplification of ground motion at intermediate distances due to reflections from the Moho surface, near-field directivity, and hanging wall effects—these filters have not been developed yet. Each filter (existing and new) utilized in our model is briefly explained in the following sections.

FILTER G_1: MAGNITUDE AND STYLE OF FAULTING SCALING

The following scaling function models the magnitude and style of faulting scaling:

$$G_1(M, F) = [c_1 \arctan(M + c_2) + c_3]F \tag{4}$$

where c_1, c_2, and c_3 are the estimator coefficients, and F represents ground motion amplitude scaling due to style of faulting. This scaling function reflects the saturation of ground motion

PGA = G_1 = Magnitude and Style of Faulting Scaling **x** G_2 = Core Attenuation Equation **x** G_3 = Basin Effect and Far Distance Correction **x** G_4 = Site Correction

$$ln(PGA) = \overbrace{ln[A(M,F)]}^{G_1} - \overbrace{0.5ln[(1-r_2)^2 + 4D_2^2 r_2]}^{G_2} - \overbrace{0.5ln[(1-\sqrt{r_3})^2 + 4D_3^2\sqrt{r_3}]}^{G_3} + \overbrace{b_v ln(V_{S30}/VA)}^{G_4} + \sigma_{ln(PGA)}$$

where,

$$r_2 = R_{rup} / R_2 \quad r_3 = R_{rup} / R_3$$

$$A(M,F) = [c_1 \arctan(M + c_2) + c_3]\ F$$

$$R_2 = c_4 M + c_5$$

$$D_2 = c_6 \cos[c_7(M + c_8)] + c_9$$

c_1	c_2	c_3	c_4	c_5	c_6	c_7	c_8	C_9	b_v	VA	R_1	$\sigma_{ln(PGA)}$
0.14	-6.25	0.37	2.237	-7.542	-0.125	1.19	-6.15	0.525	-0.24	484.5	100	0.552

Note: To capture basin effect it is recommended to set $D_1 = 0.35$, otherwise $D_1 = 0.65$
$F = 1$ for strike-slip and normal faulting; $F = 1.28$ for reverse faulting
R_{rup} = Closest fault distance, and M = Moment magnitude

Figure 2. GK-07 ground motion prediction equation for free-field horizontal component of ground motion (Graizer and Kalkan 2007).

amplitudes with increasing magnitudes. According to the results of Sadigh et al. (1997), reverse fault events create ground motions approximately 28% higher than those from crustal strike-slips. Following this, we used $F = 1$ for strike-slip and normal faults and $F = 1.28$ for reverse faults.

FILTER G_2: CORE ATTENUATION EQUATION

As compared to the other GMPEs, one of the unique features of the GK-07 is that it models an increase in ground motion amplitude (bump or sudden decay point on attenuation curve) at certain distances (about 3–10 km) from the fault rupture. Figure 3a shows an example of the bump on the attenuation curve at the near-field of the 2004 M6.4 Parkfield earthquake. This phenomenon is modeled by the core attenuation function, as shown in Equation 5:

$$G_2(M, R_{rup}) = \frac{1}{\sqrt{\left[1 - (R_{rup}/R_2)\right]^2 + 4D_2^2(R_{rup}/R_2)}} \tag{5}$$

$$\begin{aligned} R_2 &= c_4 M + c_5 \\ D_2 &= c_6 \cos(c_7 M + c_8) + c_9 \end{aligned} \tag{6}$$

where R_2 and D_2 (originally denoted as R_0 and D_0 in Graizer and Kalkan 2007) are the corner distance and the damping parameters, respectively. They quantify the location and intensity of the bump on the attenuation curve. The terms $c_{4\ldots9}$ in Equation 6 are the estimator

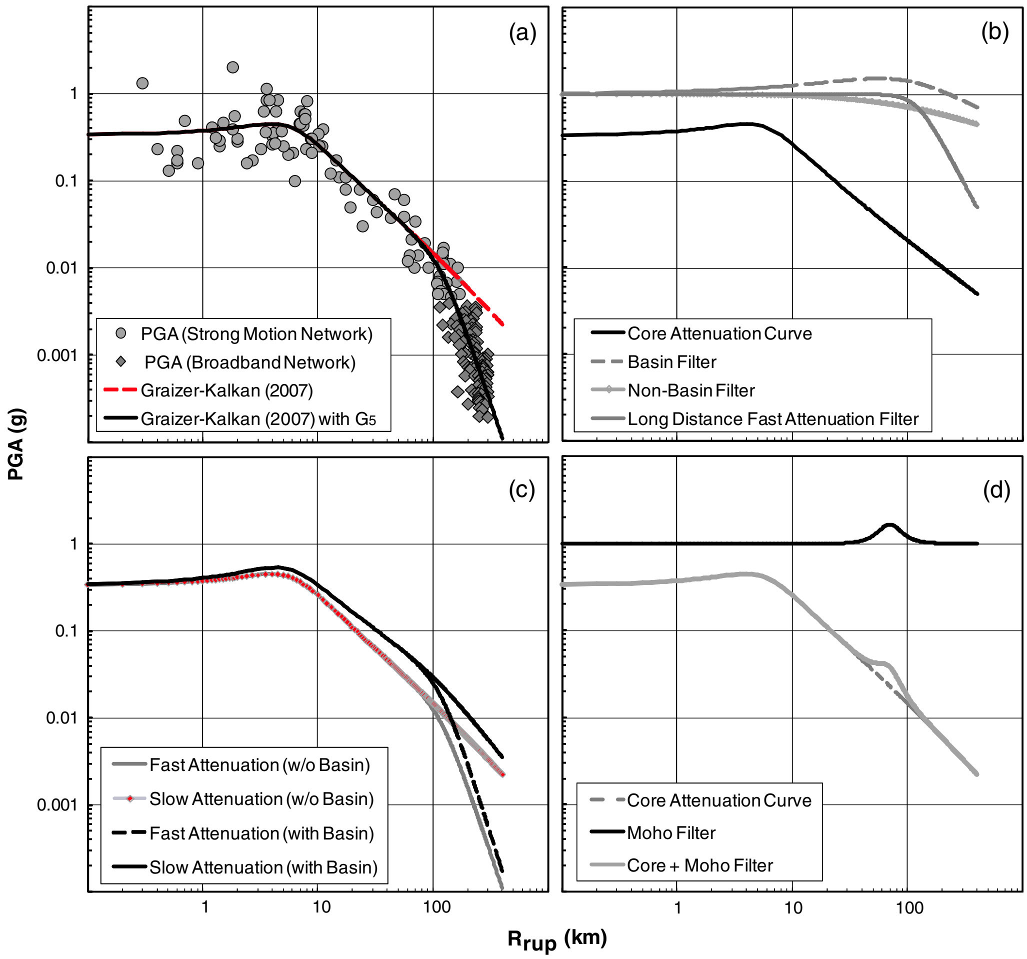

Figure 3. (a) PGA data and approximation curves for ground motion attenuation (low-amplitude data shows faster attenuation) for the 2004 M6.0 Parkfield earthquake; (b) examples of filters modeling core attenuation, basin, and far-distance fast attenuation; (c) effects of basin filter and far-distance fast attenuation filter on attenuation curve; (d) modeling the Moho reflection.

coefficients. Equation 6 implies that the turning point on the attenuation curve occurs at larger distances for larger magnitudes. D_2 is a function of magnitude, producing a significant bump with $D_2 = 0.4$ for $M6 - 6.5$. $D_2 > 0.4$ for $M < 5$ and $M > 7$ produces a lower bump or no bump. The recorded data from past earthquakes shows that the relative amplitude of a bump on the attenuation curve decreases at large magnitudes ($M > 6.5$) or small magnitudes ($M < 6$). The bump saturates at $M > 7.5$ (Graizer and Kalkan 2007).

FILTER G_3: SEDIMENT DEPTH EFFECT (BASIN EFFECT)

Deep sedimentary basins (e.g., the Los Angeles, San Bernardino, and San Fernando basins) can amplify surface waves at distances 30 km to 50 km from the source

(Lee et al. 1995, Campbell 1997, Frankel et al. 2001, Hatayama and Kalkan 2011). The G_3 filter models this effect.

$$G_3(M, R_{rup}, C_3) = \frac{1}{\sqrt{\left[1 - (R_{rup}/R_3)^{0.5}\right]^2 + 4D_2^2(R_{rup}/R_3)^{0.5}}}$$

$$D_3 = \begin{cases} 0.65 \text{ for } Z < 1 \text{ km} \\ 0.35 \text{ for } Z \geq 1 \text{ km} \end{cases} \tag{7}$$

where R_3 describes the distance at which the amplification (bump on attenuation curve) due to deep sediments takes place, and D_3 defines the amplitude of amplification. Low values of D_3 produce high degrees of amplification (prominent bump). If the sediment thickness is small, basin effects can be neglected, and D_3 can be taken as 0.65. The G_3 filter with this value of D_3 results in a change of slope on the attenuation curve at distances larger than R_3 only; it remains ineffective for distances less than R_3 (Figure 3b). As shown in Figure 3c, the resultant attenuation function $(G_2 \cdot G_3)$ decays proportionally to $R_{rup}^{-1.5}$ at distances $R > R_3$, unlike R_{rup}^{-1} decay due to the G_2 filter. The damping parameter D_3 is envisioned to be a smooth function of basin depth (thickness of sediment layer). As a first approximation, the basin effect was considered to be the same for all sediment depths of more than 1 km. With increasing sediment thickness, D_3 in Equation 7 is expected to decrease smoothly from 0.65 to 0.3–0.4, and its effect on the attenuation curve saturates with an increase in sediment thickness.

FILTER G_4: EFFECT OF SHALLOW SITE CONDITIONS

A cross-comparison of NGA GMPEs demonstrates significant differences in site amplification for PGA and spectral acceleration ordinates for soft-soils ($V_{S30} < 400$ m/s), therefore calling for further calibration of nonlinear models using experimental data (2009 SSA presentation of Prof. Idriss). Because of the large variability in nonlinear models, and on the basis of available studies (a list of references is given in Graizer and Kalkan 2007), a linear site amplification filter was adopted:

$$G_4(V_{S30}) = b_v \cdot ln(V_{S30}/V_A) \tag{8}$$

Equation 8 is an equivalent form of the linear site correction formula given in Boore et al. (1997), where $b_v = -0.371$, whereas our estimates yield $b_v = -0.24$. With its parameters given in Figure 2, Equation 8 is similar to Field (2000), exhibiting less amplification than that of Boore et al. (1997) as V_{S30} decreases.

FILTER G_5: FAR DISTANCE ATTENUATION FILTER

For distances more than 100 km from a fault (but increasing with increase in M), attenuation of global ground motion data demonstrates two main tendencies: faster attenuation on the order of R_{rup}^{-4} in areas of relatively low Q and slower attenuation on the order of $R_{rup}^{-1.5}$ in areas of relatively high Q. For regions similar to the central and eastern United States with relatively high Q (Singh and Herrmann 1983, Mitchell and Hwang 1987, Chandler et al. 2006), the attenuation rate at the far-field is about the same as in the near-field (about

$R_{rup}^{-1.5}$). In the western United States, with relatively low Q, attenuation is faster (almost R_{rup}^{-4}) at the far-field. A good example of this is the 2004 Parkfield earthquake shown in Figure 3a, where the ground motion attenuates much faster beyond 100 km.

To model fast attenuation at far distances, the following filter is developed:

$$G_5(M, R_{rup}) = \frac{1}{\sqrt{\left[1 - (R/R_5)^d\right]^2 + 4D_5^2(R/R_5)^d}} \tag{9}$$

$$R_5 = c_{11}M^2 + c_{12}M + c_{13}$$

The G_5 filter has a flat response at distances $R_{rup} < R_5$ and a turning point around the corner distance R_5 for damping parameter $D_5 = 0.6 - 0.7$. The slope of the attenuation curve is determined by an adjustable parameter d, which varies from 0 to 2.5; 0 means no adjustment to attenuation slope. R_5 increases with M. The use of G_5 brings the attenuation slope at far distances to R_{rup}^{-2}. We found that $d = 0.5$ provides a reasonable attenuation rate averaged at the far-field. Increasing d yields a faster attenuation, as it may be taken as 0.8–1.2 for regions with very low Q.

COMPARISON OF PREDICTIONS WITH RECORDED DATA

The PGA data of the Global Atlas database are categorized into 18 magnitude bins having a magnitude interval of 0.2. The predictions due to the GK-07 are compared with the recorded data in each bin in Figures 4 and 5. V_{S30} of predictions is taken as 400 m/s as the average value of the database. As shown, the GK-07 fits well to recorded data up to a 100-km distance, indicating that our core attenuation equation is a good approximation of ground motion attenuation for a range of magnitudes. In order to achieve a better fit at intermediate distance ranges ($20 < R_{rup} < 100$ km), the magnitude-dependent corner distance parameter between relatively flat attenuation and faster attenuation regions, R_2, is modified. As opposed to its initial value based on the extended NGA database, the Atlas database requires a slightly larger value. The new c_4 and c_5 parameters defining R_2 are computed as 3.67 and –12.42, respectively.

To enhance far distance predictions (>100 km), where faster attenuation is generally observed, the G_5 filter was utilized. The new GMPE including the modified R_2 and additional far-distance filter is called "GKL-13," and its estimator coefficients are presented in Figure 6.

The predictive power of the GKL-13 is compared against the GK-07 and also against the recorded data in Figures 4 and 5. Both GMPEs yield similar predictions between 0 km and 100 km. The differences—slightly higher predicted PGA derived from the GK-07 in the near-field and slightly lower predicted PGA in the far-field—are associated with the first term c_{10} added to the G_5 filter. Without this scaling term, both GMPEs would produce exactly the same results up to 100 km. This scaling term helped to remove the slight distance bias observed in predictions (discussed further in the next section). It is evident that the G_5 filter leads to enhanced predictions in the near-, mid-, and far-field.

Figures 4 and 5 also compare our predictions with a commonly used NGA relation of Campbell and Bozorgnia (2008), which is denoted as "CB-08." As compared to the CB-08,

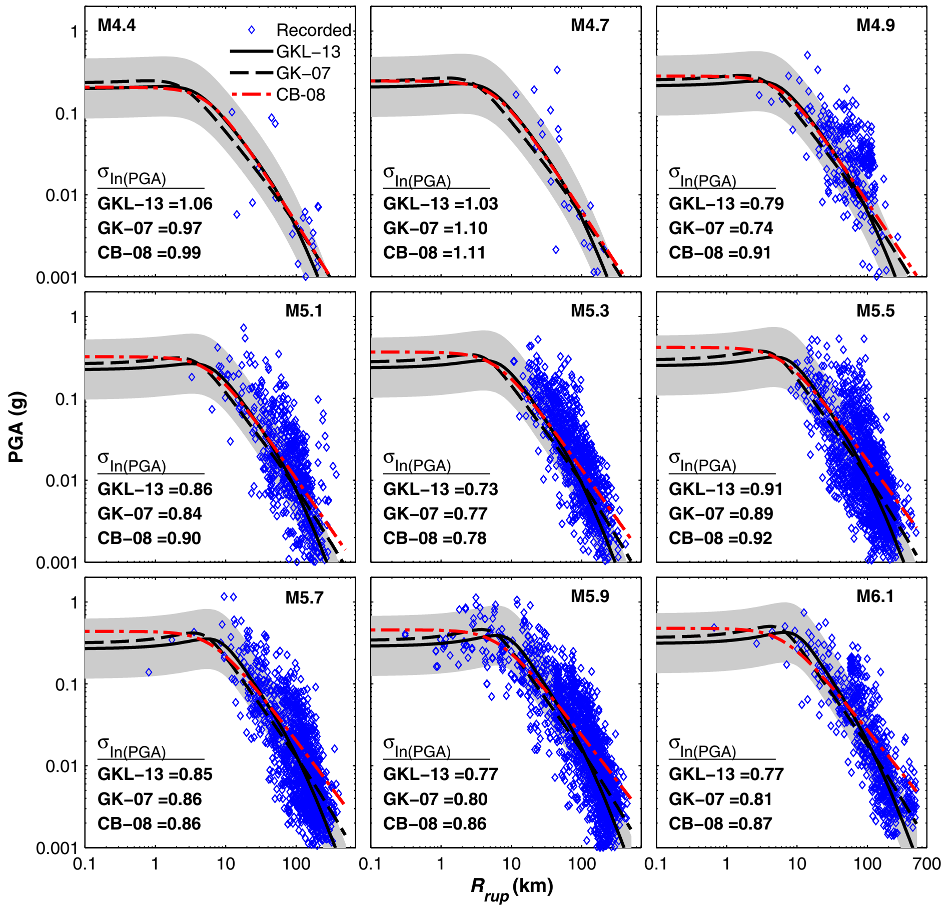

Figure 4. Comparison of GK-07 and GKL-13 GMPEs for $4.2 \le M \le 6.1$; data are divided into magnitude bins with magnitude interval of 0.2; gray zones are bounded by $\pm\,\sigma$ of predictions. Also shown is the CB-08 GMPE.

both GK-07 and GKL-13 result in comparable predictions within 100 km and better predictions at larger distances for a range of magnitudes. The CB-08 overestimates ground motion data at large distances ($R_{rup} > 100$ km), where the predictions from the GKL-13 are much closer to the observations. In all these comparisons, the maximum horizontal components of ground motions were used. The PGA predictions of the CB-08, originally predicting the geometric mean, were amplified by 1.12; this adjustment factor was adapted from Campbell and Bozorgnia (2007).

The performance of the GKL-13 is further demonstrated in Figure 7, where the PGA predictions are compared with ground motion data from two damaging earthquakes: the 2008 *M*7.9 Wenchuan (China) and 2009 *M*6.3 L'Aquilla (Italy) events. The predictions from the GKL-13 are for the average V_{S30} of each dataset. The 16th and 84th percentile

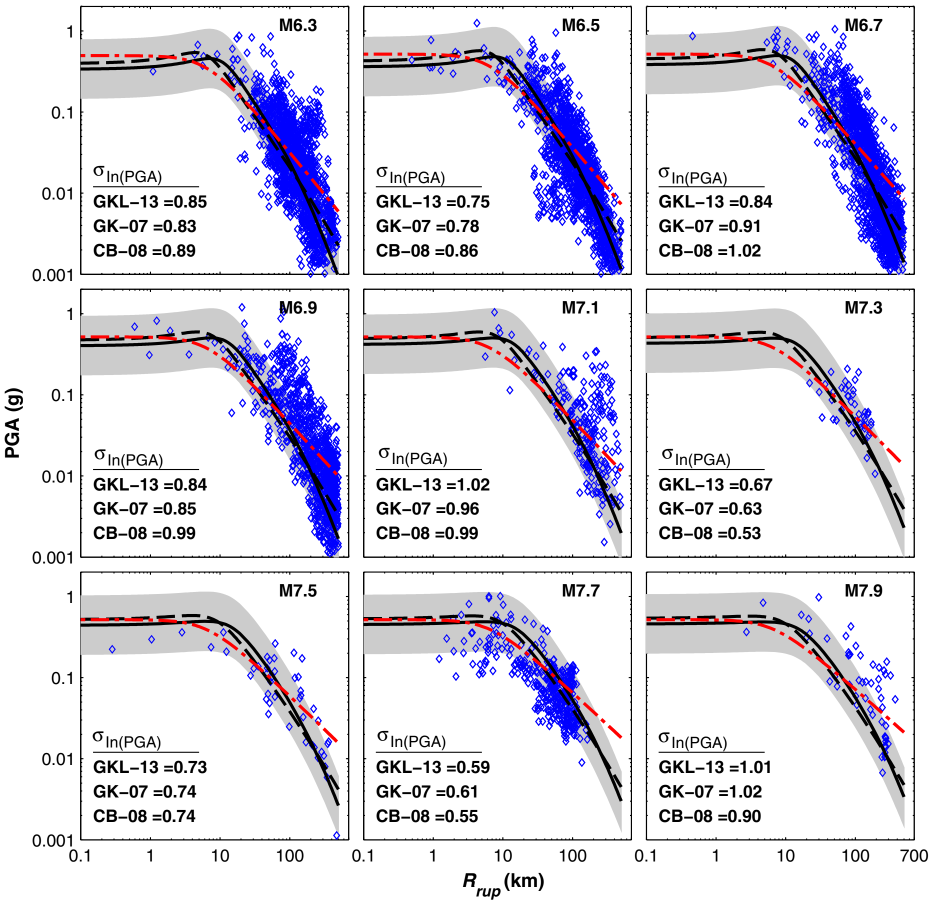

Figure 5. Comparison of GK-07 and GKL-13 GMPEs for $6.2 \leq M \leq 8.0$; data are divided into magnitude bins with magnitude interval of 0.2 gray zones are bounded by $\pm$ σ of predictions. Also shown is the CB-08 GMPE.

of the predictions bound the gray zones. At the far-field, the Wenchuan earthquake data demonstrate slow attenuation, as opposed to fast attenuation during the 2009 *M*6.3 L'Aquilla, Italy, earthquake. For both events, the GKL-13 clearly results in PGA predictions much closer to the recorded data.

RESIDUAL ANALYSIS

We have computed the standard error ($\sigma_{\ln Y}$ or simply σ) of predictions as

$$\sigma = \left[\sum (x_i - x_i')^2/(n-p)\right]^{0.5} \tag{10}$$

where x_i denotes the i^{th} value of observation, and x_i' is its prediction. $(x_i - x_i')$ is the residual of the i^{th} observation, and p is the number of dependent parameters of estimation. σ of the

PGA = **G₁** Magnitude and Style of Faulting Scaling **x** **G₂** Core Attenuation Equation **x** **G₃** Basin Effect Filter **x** **G₄** Site Correction Filter **x** **G₅** Far Distance Filter

$$ln(PGA) = ln(G_1) + ln(G_2) + ln(G_3) + ln(G_4) + ln(G_5) + \sigma_{ln(PGA)}$$

Modules

$$ln(G_1) = ln\left([c_1 \arctan(M + c_2) + c_3]\ F\right)$$

$$ln(G_2) = -0.5ln[(1-r_2)^2 + 4D_2^2 r_2]$$

$$ln(G_3) = -0.5ln[(1-\sqrt{r_3})^2 + 4D_3^2\sqrt{r_3}]$$

$$ln(G_4) = b_v ln(V_{S30}/VA)$$

$$ln(G_5) = c_{10} - 0.5ln\left[(1-\sqrt{R_{rup}/R_5})^2 + 4D_5^2\sqrt{R_{rup}/R_5}\right]$$

where,

$$r_2 = R_{rup}/R_2$$

$$R_2 = c_4 M + c_5 \qquad D_2 = c_6 \cos[c_7(M + c_8)] + c_9$$

$$r_3 = R_{rup}/R_3 \qquad R_3 = 100 \qquad D_3 = \begin{cases} 0.65 \text{ for } Z < 1 \text{ km} \\ 0.35 \text{ for } Z \geq 1 \text{ km} \end{cases}$$

$$R_5 = c_{11}M^2 + c_{12}M + c_{13}$$

Estimator Coefficients

c_1	c_2	c_3	c_4	c_5	c_6	c_7	c_8	c_9
0.14	-6.25	0.37	2.237	-7.542	-0.125	1.19	-6.15	0.525

c_{10}	c_{11}	c_{12}	c_{13}	D_5	b_v	VA	R_3	$\sigma_{\ln(PGA)}$
-0.16	18.04	-167.9	476.3	0.7	-0.24	484.5	100	0.55

Note: To capture basin effect it is recommended to set $D_3 = 0.35$, otherwise $D_3 = 0.65$
F = 1 for strike-slip and normal faulting; F = 1.28 for reverse faulting
R_{rup} = Closest fault distance, and M = Moment magnitude

Figure 6. GKL-13 global ground motion prediction equation for free-field horizontal component of ground motion.

GK-07 relation based on the extended NGA database is 0.55. For the Global Atlas database, the GK-07 and GKL-13 yield larger σ values of 0.85 and 0.83, respectively. Thus, the gray zones in Figures 4 and 5, bounded by the 16th and 84th percentile of the predictions, are practically the same for both versions of this GMPE using the Atlas database. Because most of the data fall within the gray zones, the GMPE predictions are reasonable. Although Equation 10 implies that σ has a tendency to reduce as the number of data points (n) increases, σ actually increases because of the larger variability in the Global Atlas database as opposed to the well-constrained NGA database. The difference between the two databases in terms of variability is shown in Figure 8, where the normal probability distribution function for the natural log of PGA demonstrate larger scattering of the Global Atlas database.

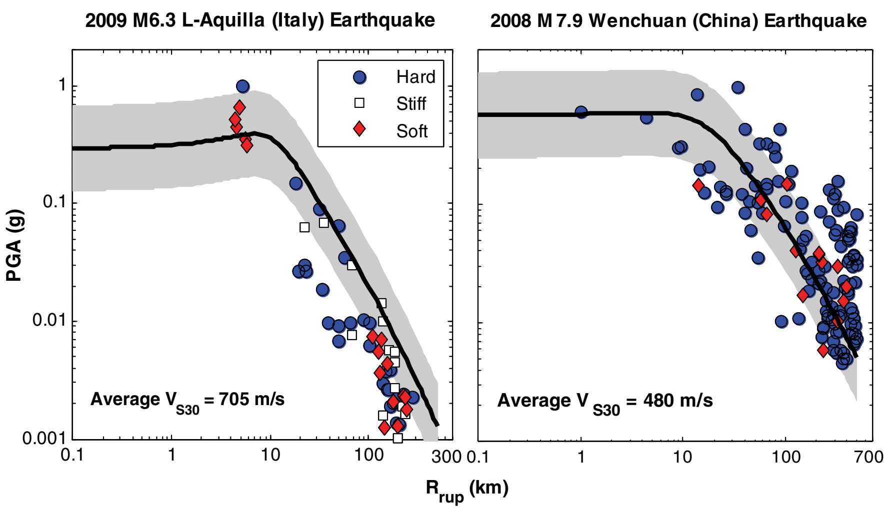

Figure 7. Ground motion predictions by the GKL-13 prediction equation for the *M*6.3 Central Italy L'Aquila earthquake (left) and for the *M*7.9 Wenchuan, China, earthquake (right); data show slow attenuation of ground motion for the Wenchuan earthquake as opposed to fast attenuation of ground motion for the L'Aquilla earthquake; the GKL-13 predictions are for an average V_{S30} of each dataset.

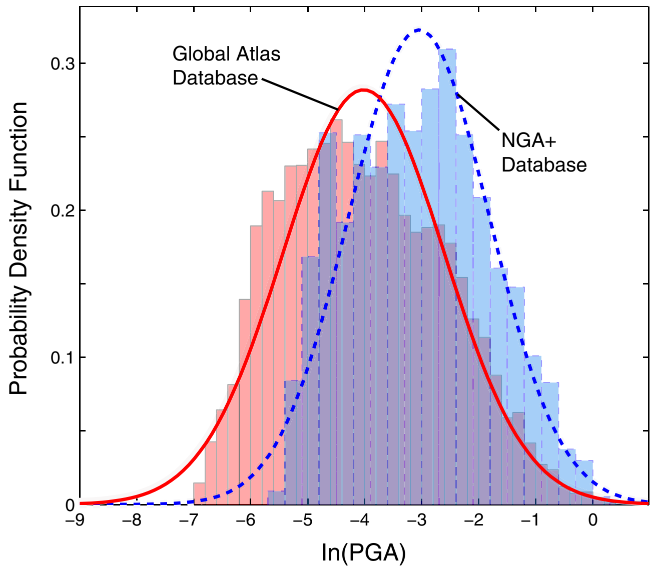

Figure 8. Probability distribution function for PGA in the extended NGA (denoted as NGA+) and Global Atlas databases.

In addition to the total σ on the basis of the entire Global Atlas database, the variation of σ within each magnitude bin is computed to examine the stability of the GMPEs at different magnitude levels. The σ due to the three GMPEs computed for each magnitude bin (as identified in Figures 4 and 5) are plotted in Figure 9a. The GK-07 and GKL-13 demonstrate a similar level of σ, slightly lower than that of the CB-08. For all GMPEs, σ demonstrates very weak linear dependence on magnitude, weaker than that reported by Strasser et al. (2009). The dependence of σ on distance was similarly examined by creating 25 distance bins with an equal distance spacing of 20 km. The variation of σ with respect to the average distance value of each bin is shown in Figure 9b. As in the case of variation with magnitude, σ demonstrates a relatively weak linear dependence on distance; it decreases when the distance is increased. Assuming a linear dependence of σ on both magnitude and distance results in the following expressions:

$$\begin{aligned} \sigma(M) &= -0.043M + 1.10 \\ \sigma(R_{rup}) &= -0.0004R_{rup} + 0.89 \end{aligned} \tag{11}$$

In order to investigate whether our predictions are biased against any independent parameter of estimations, the residuals of the predictions against M, R_{rup}, and V_{S30} are plotted in Figure 10. The GK-07 shows a slight distance bias at far-field (predicted PGA exceeds observed PGA) and no bias with respect to the magnitude and V_{S30}. Note that the GK-07 is developed using data up to 250 km; the overprediction trend at greater distances (>250 km) is due to the faster attenuation of low-amplitude data, which is not part of the NGA database (see Figure 1). Using an additional G_5 filter in the GKL-13, we were able to eliminate the far-field distance bias. Like the GK-07, GKL-13 does not show any bias with respect to magnitude or V_{S30}.

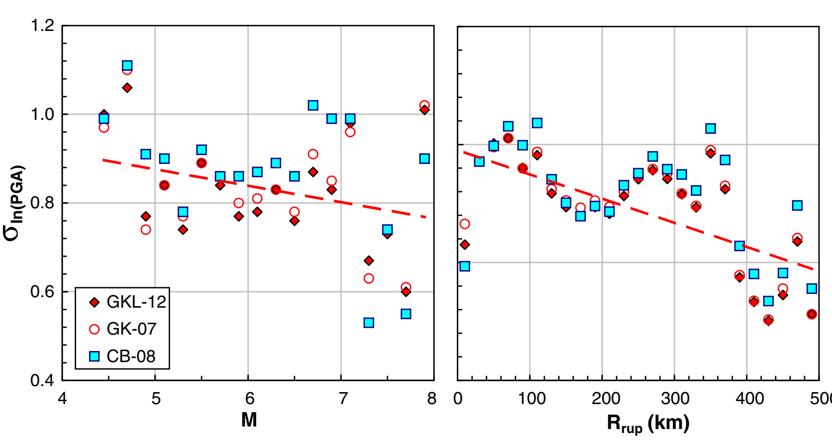

Figure 9. Variation of standard error of prediction with respect to magnitude M (left) and closest fault distance R_{rup} (right) for three ground-motion prediction equations (GKL-13, GK-07, and CB-08). Ground motion data are binned using a magnitude interval of 0.2 and distance interval of 20 km.

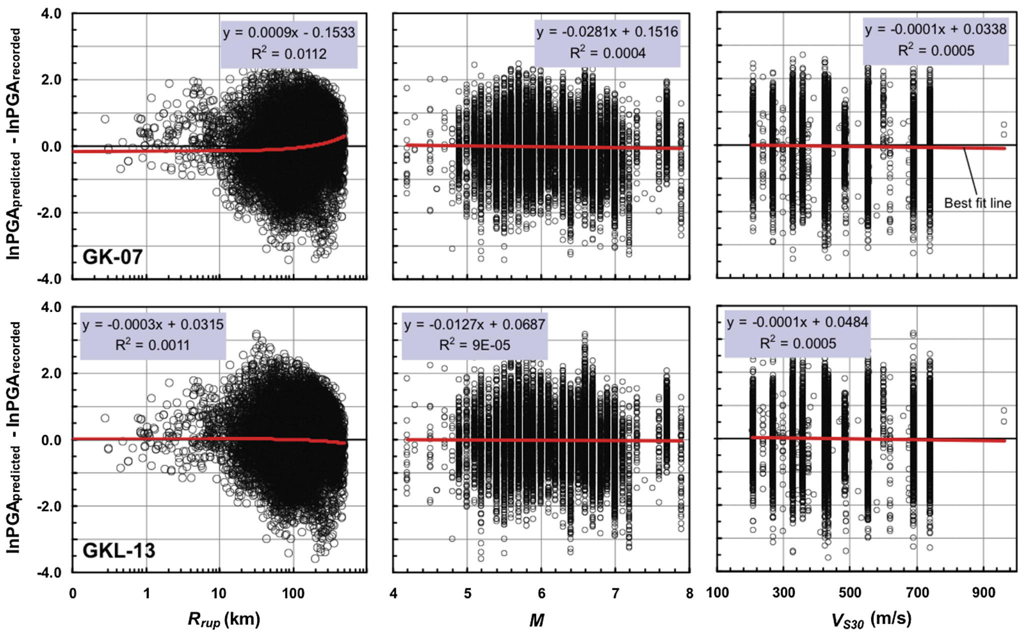

Figure 10. Distribution of residuals with respect to closest fault distance (R_{rup}), magnitude (M) and shear-wave velocity (V_{S30}) for GK-07 (top row) and for GKL-13 (bottom row) ground-motion prediction equations.

SUMMARY

There is a need for globally applicable ground motion prediction models (GMPEs) for seismic hazard assessment of regions lacking a sufficient number of strong motion observations. The objective of this study is to test the predictive power of the GK-07 against the PGA from worldwide shallow crustal events. For this objective, the most comprehensive global database, constituting of about 14,000 data points, was compiled. The test results have demonstrated that ground motion attenuation for distances greater than 100 km has two main tendencies: fast attenuation on the order of R_{rup}^{-4} and slow attenuation on the order of $R_{rup}^{-1.5}$, depending on the value of Q. For regions similar to the central and eastern United States, with relatively high Q, the ground motion attenuation rate is about $R_{rup}^{-1.5}$ at intermediate and far-field. For the western United States, with relatively low Q, the attenuation slope at distances greater than 100 km is much higher (almost R_{rup}^{-4}). By modifying two estimator coefficients in our earlier model (GK-07) and adding a new filter (G_5) to model faster attenuation, we were able to obtain a better match between recorded and predicted PGA values to distances of about 500 km. The new model (GKL-13) does not show any bias against M, R_{rup}, or V_{S30}.

The filter-based ground motion prediction modeling as presented here for shallow crustal regions can be used for other tectonic regions where subduction and intraplate events dominate the seismic hazard. A number of filters, including the core attenuation filter, basin effect filter, and far-distance filter, are expected to be applicable for such regions.

The GKL-13 presented here can be used together with our PGA-based predictive model for the calculation of spectral acceleration response ordinates. This model, as described in Graizer and Kalkan (2009), utilizes PGA as a proxy to scale the spectral shape, which is not defined as a discrete function (as in all other GMPEs). Rather, it is defined as a continuous function of spectral period.

DATA AND RESOURCES

The GK-07 and GKL-13 ground motion prediction equations are available in Fortran, Microsoft Excel, and MatLAB platforms upon request from the authors.

ACKNOWLEDGMENTS

We wish to thank Professor Izzat Idriss for providing us the results of his study, which he presented during the SSA annual meeting in 2009. Special thanks are extended to Brad Aagard, Christopher Stephens, and Shojiro Kataoka for their reviews of this paper, and to Peter Stauffer for his edits.

DISCLAIMER

Any opinions, findings, and conclusions expressed in this paper are those of the authors and do not necessarily reflect the views of the U.S. Nuclear Regulatory Commission.

REFERENCES

Akkar, S., Aldemir, A., Askan, A., Bakır, S., Canbay, E., Demirel, O., Erberik, A., Gülerce, Z., Gülkan, P., Kalkan, E., Prakash, S., Sandıkkaya, A., Sevilgen, V., Ugurhan, B., and Yenier, E., 2011. 8 March 2010 Elazıg-Kovancılar (Turkey) earthquake: Observations on ground motions and building damage, *Seismol. Res. Lett.* **82**, 42–58.

Abrahamson, N. A., and Silva, W. J., 1997. Empirical response spectral attenuation relations for shallow crustal earthquakes, *Seismol. Res. Lett.* **68**, 94–127.

Boore, D. M., 2003. Simulation of ground motion using the stochastic method, *Pure and Applied Geophysics* **160**, 635–676.

Boore, D. M., Joyner, W. B., and Fumal, T. E., 1997. Equations for estimating horizontal response spectra and peak acceleration from western North American earthquakes: A summary of recent work, *Seismol. Res. Lett.* **68**, 128–153.

Campbell, K. W., 1997. Empirical near-source attenuation relationships for horizontal and vertical components of peak ground acceleration, peak ground velocity, and pseudo-absolute acceleration response spectra, *Seismol. Res. Lett.* **68**, 154–179.

Campbell, K. W., and Bozorgnia, Y., 2007. Campbell-Bozorgnia NGA ground relations for the geometric mean horizontal component of peak and spectral ground motion parameters, Report PEER 2007/02, 240 pp.

Campbell, K. W., and Bozorgnia, Y., 2008. NGA ground motion model for the geometric mean horizontal component of PGA, PGV, PGD and 5% damped linear elastic response spectra for periods ranging from 0.01 to 10 s, *Earthquake Spectra* **24**, 139–172.

Çelebi, M. P., Bazzurro, L., Chiaraluce, P., Clemente, L., Decanini, A., DeSortis, W., Ellsworth, A., Gorini, Kalkan, E., Marcucci, G., Milana, F., Mollaioli, M., Olivieri, D., Rinaldis, A., Rovelli, F., Sabetta, and C. Stephens., 2010. Recorded motions of the M_w6.3 April 6, 2009 L'Aquila (Italy) earthquake and implications for building structural damage, *Earthquake Spectra* **26**, 651–684.

Chandler, A. M., Lam, N. T. K., and Tsang, H. H., 2006. Near-surface attenuation modeling based on rock shear-wave velocity profile, *Soil Dynamics and Earthquake Engineering* **26**, 1004–1014.

Field, E. H., 2000. A modified ground motion attenuation relationship for Southern California that accounts for detailed site classification and a basin-depth effect, *Bull. Seism. Soc. Amer.* **90**, 209–221.

Frankel, A., Carver, D., Cranswick, E., Bice, T., Sell, R., and Hanson, S., 2001. Observation of basin ground motions from a dense seismic array in San Jose, California, *Bull. Seism. Soc. Am.*, **91**, 1–12.

Fukushima, Y., and Tanaka, T., 1990. A new attenuation relation for peak horizontal acceleration of strong earthquake ground motion in Japan, *Bull. Seism. Soc. Am.*, **80**, 757–783.

Graizer, V., and Kalkan, E., 2007. Ground motion attenuation model for peak horizontal acceleration from shallow crustal earthquakes, *Earthquake Spectra* **23**, 585–613.

Graizer, V., and Kalkan, E., 2009. Prediction of response spectral acceleration ordinates based on PGA attenuation, *Earthquake Spectra* **25**, 39–69.

Graizer, V., and Kalkan, E., 2011. Modular filter-based approach to ground motion attenuation modeling, *Seism. Res. Letters* **82**, 21–31.

Hatayama, K., and Kalkan, E., 2011. Long-period (3 to 10 s) ground motions in and around the Los Angeles Basin during the M_w7.2 El-Mayor Cucapah earthquake of April 4, 2010, in *Proc. of the 4th IASPEI / IAEE International Symposium*, 23–26 August 2011, University of California Santa Barbara, available at http://nsmp.wr.usgs.gov/ekalkan/PDFs/A72_Hatayama_Kalkan.pdf.

Joyner, W. B., 2000. Strong motion from surface waves in deep sedimentary basins, *Bull. Seism. Soc. Am.* **90**, 95–112.

Lee, V. W., Trifunac, M. D., Todorovska, M. I., and Novikova, E. I., 1995. Empirical equations describing attenuation of peak of strong ground motion, in terms of magnitude, distance, path effects and site conditions, *USC report no. CE 95-02*, 268 pp.

Mitchell, B. J., and Hwang, H. J., 1987. Effect of low Q sediments and crustal Q on Lg attenuation in the United States, *Bull. Seism. Soc. America* **77**, 1197–1210.

Sadigh, K., Chang, C.-Y., Egan, J. A., Makdisi, F., and Youngs, R. R., 1997. Attenuation relationships for shallow crustal earthquakes based on California strong motion data, *Seismol. Res. Lett.* **68**, 180–189.

Segou, M., and Kalkan, E., 2011. Ground Motion Attenuation during M7.1 Darfield and M6.3 Christchurch (New Zealand) earthquakes and performance of global predictive models, *Seismol. Res. Lett.* **82**, 866–874.

Singh, S., and Herrmann, R. B., 1983. Regionalization of crustal coda Q in the continental United States, *J. Geophys. Res.* **88**, 527–538.

Strasser, F. O., Abrahamson, N. E., and Bommer, J. J., 2009. Sigma: Issues, insights, and challenges, *Seismol. Res. Lett.* **80**, 40–56.

(Received 2 November 2009; accepted 27 June 2012)

No.	Location	Mw	Num. of Data	Style of Faulting
1	Adana-Ceyhan, Turkey	6.3	9	Strike-Slip
2	Altinsac, Turkey	5.5	1	Reverse
3	Anchialos, Greece	5.6	2	Normal
4	Anza	5.2	101	Strike-Slip
5	Anza, California	5.6	3	Undefined
6	Ardakul, Iran	7.2	1	Strike-Slip
7	Ardebil, Iran	6.1	19	Strike-Slip
8	Arthurs Pass, New Zealand	6.7	18	Strike-Slip
9	Athens, Greece	6	1	Normal
10	Azores, Portugal	5.9	4	Strike-Slip
11	Baiano, Italy	4.9	2	Undefined
12	Baja California, Mexico	5.1	36	Strike-Slip
13	Baja California, Mexico (Aftersho	5	23	Undefined
14	Bam, Iran	6.6	1	Strike-Slip
15	Banja Luka, Bosnia and Herzego	5.7	4	Strike-Slip
16	Basilicata, Italy	5.2	1	Undefined
17	Bhuj, India (Aftershock)	5.3	1	Undefined
18	Big Bear City	5.2	91	Strike-Slip
19	Big Bear, California	6.5	26	Strike-Slip
20	Biga, Turkey	6.1	5	Strike-Slip
21	Bingol, Turkey	6.3	4	Strike-Slip
22	Bitola, Macedonia	5.6	2	Undefined
23	Boolarra, Australia	4.2	14	Undefined
24	Borrego Mountain, California	6.6	1	Strike-Slip
25	Boumerdes, Algeria	6.8	13	Reverse
26	Bovec, Slovenia	5.6	13	Strike-Slip
27	Brijezde, Serbia	5.5	1	Strike-Slip
28	Calabria, Italy	5.2	2	Normal
29	Cape Campbell, New Zealand	6.1	30	Normal
30	Cass, New Zealand	6.1	11	Strike-Slip
31	Chahar Mahal Bakhtiari, Iran	6	1	Strike-Slip
32	Chalfant Valley, California	6.2	6	Strike-Slip
33	Chalfant Valley, California (After	5.7	5	Reverse
34	Chalfant Valley, California (Fore	5.8	4	Normal
35	Chamoli, India	6.5	11	Reverse
36	Changureh-Avaj, Iran	6.5	62	Reverse
37	Charles Sound, New Zealand	6.1	1	Reverse
38	Chenoua, Algeria	5.9	3	Reverse
39	Chi-Chi, Taiwan	7.7	407	Reverse
40	Chi-Chi, Taiwan (Aftershock)	6.6	1096	Reverse
41	Chino Hills, California	5.4	462	Undefined
42	Chios, Greece	5.6	2	Strike-Slip
43	Coalinga, California	6.3	53	Reverse

(*continued*)

No.	Location	Mw	Num. of Data	Style of Faulting
44	Coalinga, California (Aftershock)	5.1	7	Reverse
45	Coast of Guerrero, Mexico	5.8	4	Reverse
46	Coast of Northern California	7.2	8	Strike-Slip
47	Corinth, Greece	6.6	2	Normal
48	Corinth, Greece (Aftershock)	6.3	1	Normal
49	Cosenza, Italy	4.8	1	Undefined
50	Coyote Lake, California	5.7	2	Strike-Slip
51	Cyprus	6.8	1	Strike-Slip
52	Dahuiyeh, Iran	6.4	21	Reverse
53	Dead Sea, Israel	5.1	3	Strike-Slip
54	Denali, Alaska	7.9	24	Strike-Slip
55	Dharmsala, India	5.5	9	Reverse
56	Dillon, Montana	5.6	7	Normal
57	Dinar, Turkey	6.4	7	Normal
58	Doubtful Sound, New Zealand	6.4	2	Reverse
59	Duzce, Turkey	7.1	1	Strike-Slip
60	Duzce, Turkey (Aftershock)	6	3	Reverse
61	East Cape, New Zealand	7.1	15	Normal
62	Edgecumbe, New Zealand	6.5	2	Normal
63	Edgecumbe, New Zealand (Afte	5.8	1	Undefined
64	Ellalong, Australia	4.7	9	Undefined
53	Elmore Ranch, California	6	1	Strike-Slip
54	Epagny, France	4.3	3	Undefined
55	Erzincan, Turkey	6.6	3	Strike-Slip
56	Eureka, California	7	2	Strike-Slip
57	Faial Island, Portugal	6.1	5	Strike-Slip
58	Filippias, Greece	5.5	5	Reverse
59	Fiordland, New Zealand	5.8	10	Reverse
60	Firuzabad, Iran	5.9	9	Strike-Slip
61	Friuli, Italy	6.5	22	Reverse
62	Friuli, Italy (Aftershock)	5.9	18	Undefined
63	Friuli, Italy (Foreshock)	5.5	15	Undefined
64	Fukuoka, Japan	6.6	271	Strike-Slip
65	Garmkhan, Iran	6.5	10	Strike-Slip
66	Gazli, Uzbekistan	6.7	1	Reverse
67	Geiyo, Japan	6.8	316	Normal
68	Gisborne, New Zealand	5.6	4	Undefined
69	Godley River, New Zealand	6.1	1	Strike-Slip
70	Golbaf, Iran	6.6	5	Strike-Slip
71	Golbasi, Turkey	6	3	Strike-Slip
72	Golcayir, Turkey	6	1	Normal
73	Griva, Greece	6.1	6	Normal
74	Guerrero, Mexico	6.9	151	Reverse

(*continued*)

No.	Location	Mw	Num. of Data	Style of Faulting
75	Gulf of Akaba, Saudi Arabia	7.2	7	Strike-Slip
76	Gulf of Akaba, Saudi Arabia (Aft	5.7	1	Strike-Slip
77	Gulf of California, Mexico	5.7	2	Strike-Slip
78	Haciveliler, Turkey	4.8	2	Undefined
79	Hastings, New Zealand	5.6	1	Normal
80	Hawkes Bay, New Zealand	5.4	2	Normal
81	Hawks Crag, New Zealand	5.8	22	Reverse
82	Hector Mine, California	7.1	105	Strike-Slip
83	Hector Mine, California (Aftersho	5.7	69	Undefined
84	Hendek-Akyazi, Turkey	5.3	8	Strike-Slip
85	Hokkaido, Japan	7	356	Reverse
86	Hokkaido, Japan (Aftershock)	6.7	355	Reverse
87	Honeydew, California	6.1	4	Reverse
88	Honshu, Japan	6.6	2416	Reverse
89	Horasan-Narman, Turkey	6.6	1	Strike-Slip
90	Hualien, Taiwan	6.2	36	Reverse
91	Hyuga-Nada #2, Japan	6.7	121	Reverse
92	Ibaraki Prefecture, Japan	5.4	199	Reverse
93	Imotski-Grude, Croatia	5.6	1	Undefined
94	Imperial Valley, California	6.5	38	Strike-Slip
95	Inangahua, New Zealand	7.2	15	Undefined
96	India-Bangladesh Border	5.8	18	Strike-Slip
97	India-Burma Border	7.2	33	Reverse
98	India-Burma Border	5.9	11	Strike-Slip
99	Ionian, Greece	5.4	1	Undefined
100	Irpinia, Italy	6.9	1	Normal
101	Ishakli, Turkey	6.5	7	Normal
102	Ishakli, Turkey (Aftershock)	5.8	5	Normal
103	Itea, Greece	5.6	4	Normal
104	Iwate, Japan	6.9	395	Undefined
105	Izmir, Turkey	6	5	Strike-Slip
106	Joshua Tree, California	6.2	1	Strike-Slip
107	Kagoshima, Japan	6.1	26	Strike-Slip
108	Kagoshimaen-Hoku-Seibu, Japa	6	22	Strike-Slip
109	Kalamata, Greece	6.4	8	Strike-Slip
110	Kalamata, Greece (Aftershock)	4.8	3	Undefined
111	Kallirro, Greece	5.4	1	Normal
112	Karebas, Iran	6.2	19	Strike-Slip
113	Kefallinia Island, Greece	6.9	7	Strike-Slip
114	Kefallinia Island, Greece (Afters	6.2	3	Strike-Slip
115	Kiholo Bay, Hawaii	6.7	23	Normal
116	Kiholo Bay, Hawaii (Aftershock)	6	18	Reverse
	Kobe, Japan	6.9	23	Strike-Slip

(*continued*)

No.	Location	Mw	Num. of Data	Style of Faulting
	Kocaeli, Turkey	7.6	38	Strike-Slip
	Kocaeli, Turkey (Aftershock)	5.8	76	Strike-Slip
	Kojur-Firoozabad, Iran	6.3	100	Reverse
	Kopaonik, Serbia	5.9	2	Strike-Slip
	Koyyeri, Turkey	5.2	1	Undefined
	Kozani-Grevena, Greece	6.6	10	Normal
	Kyllini, Greece	5.9	6	Strike-Slip
	Kyushu, Japan	6.4	77	Reverse
	Lake Tahoe, Nevada	5.9	1	Strike-Slip
	Lake Tennyson, New Zealand	6	3	Strike-Slip
	Landers, California	7.3	44	Strike-Slip
	L'Aquila	6.3	55	Normal
	Lazio Abruzzo, Italy	5.9	15	Normal
	Lazio Abruzzo, Italy (Aftershock)	5.5	9	Normal
	Livermore, California	5.8	9	Reverse
	Loma Prieta, California	6.9	34	Reverse
	Lytle Creek, California	5.4	1	Undefined
	Magion Oros Peninsula, Greece	6.6	3	Strike-Slip
	Mammoth Lakes, California	5.9	1	Normal
	Managua, Nicaragua	6.2	1	Undefined
	Manjil, Iran	7.4	1	Strike-Slip
	Masjed-E-Soleyman, Iran	5.6	3	Reverse
	Meckering, Australia	4.2	1	Undefined
	Meydan, Turkey	5.4	5	Normal
	Michoacan, Mexico	7.1	36	Strike-Slip
	Milford Sound, New Zealand	6.5	3	Reverse
	Milpitas, California	5.6	211	Strike-Slip
	Miyagi-Hokubu, Japan	6	199	Reverse
	Miyagi-Oki, Japan	7	364	Reverse
	Montenegro, Serbia	6.9	20	Reverse
	Montenegro, Serbia (Aftershock)	6.2	14	Reverse
	Morgan Hill, California	6.2	9	Strike-Slip
	Mt. Carmel, Illinois	5.2	11	Undefined
	Mt. Carmel, Illinois (Aftershock)	4.6	2	Undefined
	Muradiye, Turkey	7	1	Strike-Slip
	New Zealand	6.2	11	Strike-Slip
	Niigata, Japan	6.6	1	Reverse
	Niigata, Japan (Aftershock)	6.3	1684	Reverse
	Nisqually, Washington	6.8	62	Normal
	North Palm Springs, California	6	11	Reverse
	Northridge, California	6.7	71	Reverse
	Northwest China	6.1	8	Normal
	Noto Peninsula, Japan	6.7	377	Undefined

(*continued*)

No.	Location	Mw	Num. of Data	Style of Faulting
	Oaxaca, Mexico	7.1	3	Reverse
	Obsidian Butte, California	5.2	44	Strike-Slip
	Off coast of Karpathos, Greece	6.2	1	Strike-Slip
	Ormond, New Zealand	6.4	24	Strike-Slip
	Parkfield, California	6.1	232	Strike-Slip
	Parma, Italy	5	1	Reverse
	Pasinler, Turkey	5.4	1	Strike-Slip
	Patras, Greece	5.6	10	Strike-Slip
	Peru	6.6	2	Undefined
	Petrolia, California	7.2	7	Reverse
	Petrolia, California (Aftershock)	6.6	8	Strike-Slip
	Pol-e-Abgineh, Iran	5.2	6	Reverse
	Polkowice, Poland	5	1	Undefined
	Potenza, Italy	5.8	3	Strike-Slip
	Preveza, Greece	5.4	4	Reverse
	Puebla, Mexico	6.9	15	Normal
	Pulumur, Turkey	6	5	Strike-Slip
	Pyrgos, Greece	5.4	2	Strike-Slip
	Racha, Georgia	7	6	Reverse
	Racha, Georgia (Aftershock)	6.2	12	Reverse
181	Reggio nell'Emilia, Italy	5.2	2	Undefined
182	Rotorua, New Zealand	5.4	8	Strike-Slip
183	Ryukyu Islands, Japan	5.7	3	Reverse
184	Saguenay, Canada	5.8	2	Reverse
185	Sahneh, Iran	5.2	5	Reverse
186	Saint Die, France	5	8	Normal
187	Salehabad, Iran	5.5	3	Reverse
188	San Fernando, California	6.6	111	Undefined
189	San Juan Bautista, California	5.2	2	Strike-Slip
190	San Simeon	6.5	51	Reverse
191	Santa Barbara, California	5.8	3	Reverse
192	Sapanca-Adapazari, Turkey	5.6	25	Strike-Slip
193	Sarria Becerrea, Spain	4.9	1	Undefined
194	Satsop, Washington	5.8	4	Normal
195	Sea of Japan	5.9	22	Reverse
196	Secretary Island, New Zealand	6.9	5	Reverse
197	Seferihisar, Turkey	5.7	9	Strike-Slip
198	Shikoku, Japan	5.7	138	Strike-Slip
199	Sicily, Italy	5.8	7	Strike-Slip
200	Sierra Madre, California	5.6	1	Reverse
201	Southern Honshu, Japan	5.5	181	Reverse
202	Spitak, Armenia	6.7	1	Reverse
203	Strofades, Greece	6.6	10	Reverse

(*continued*)

No.	Location	Mw	Num. of Data	Style of Faulting
204	Superstition Hills, California	6.5	4	Strike-Slip
205	Sur, Lebanon	5.6	1	Undefined
206	Tabas, Iran	7.3	1	Reverse
207	Tadmuriyah, Syria	5.5	10	Strike-Slip
208	Taiwan	6.4	96	Strike-Slip
209	Tangshan, China	7.6	6	Strike-Slip
210	Tbilisi, Georgia	4.8	1	Undefined
211	Te Anau, New Zealand	6.7	2	Strike-Slip
212	Te Kuha, New Zealand	6.3	7	Strike-Slip
213	Terceira Island, Portugal	6.9	1	Strike-Slip
214	Thessaloniki, Greece	6.2	1	Normal
215	Thomson Reservoir, Australia	4.5	15	Undefined
216	Tikokino, New Zealand	5.7	10	Reverse
217	Tirana, Albania	5.9	2	Reverse
218	Tithorea, Greece	5.9	4	Normal
219	Tokachi-Oki, Japan (Aftershock)	6.7	79	Reverse
220	Tokomaru, New Zealand	5.7	2	Reverse
221	Tottori, Japan	6.7	303	Strike-Slip
222	Trinidad, California	7.3	1	Strike-Slip
223	Turkmenistan	7	12	Reverse
224	Umbria-Marche, Italy	6	26	Normal
225	Umbria-Marche, Italy (Aftershock)	5.9	49	Strike-Slip
226	Umbria-Marche, Italy (Foreshock)	5.7	19	Normal
227	Upland, California	5.7	1	Strike-Slip
228	Urmiya, Iran	5.8	1	Normal
229	Valnerina, Italy	5.8	7	Normal
230	Valparaiso, Chile (Aftershock)	7	1	Undefined
231	Victoria, Mexico	6.3	6	Strike-Slip
232	Volos, Greece	6.6	1	Normal
233	Volos, Greece (Aftershock)	6.3	1	Undefined
234	Vrancea, Romania	7.5	23	Reverse
235	Weber, New Zealand	6.4	54	Strike-Slip
236	Wells, Nevada	6	69	Normal
237	Wenchuan, China	7.9	32	Undefined
238	West of Invercargill, New Zealand	7.1	12	Reverse
239	Western Honshu, Japan	5.1	197	Reverse
240	Whittier Narrows, California	5.9	24	Reverse
241	Whittier Narrows, California (Afters	5.2	3	Strike-Slip
242	Yamaguchi, Japan	5.8	174	Strike-Slip
243	Yountville, California	5	27	Undefined
244	Yucaipa	4.9	187	Reverse